Three-dimensional buoyant hydraulic fractures: constant release from a point source
Supplemental Materials

Andreas Möri and Brice Lecampion

May 2, 2022

Contents

1 Approximated toughness dominated solution $\hat{\mathrm{K}}$

The solution of Germanovich et al. [2014] recognizes that in the toughness limit, the 3D buoyant fracture has a finger-like geometry consisting of a toughness dominated head and a viscosity dominated tail. The head has a constant volume and shape and a strictly hydrostatic net pressure, as viscous dissipation is neglected. The viscous tail has a constant breadth, the net pressure is uniform at every horizontal cross-section, and the vertical net pressure gradient is negligible compared to buoyancy.

1.1 Toughness dominated head

The shape of the head is solved numerically by Germanovich et al. [2014] such that $K_I = K_{Ic}$ all along the propagating part of the head front. A linear hydrostatic pressure is set in the head which leads to a constant and uniform breadth in its lower part. The toughness head scaling applies, in other words, the characteristic scales are:

$$b_{\hat{k}}^{\text{head}} = \ell_{\hat{k}}^{\text{head}} = \ell_b = \frac{K_{Ic}^{2/3}}{\Delta\gamma^{2/3}}, \quad w_{\hat{k}}^{\text{head}} = \frac{K_{Ic}^{4/3}}{E'\Delta\gamma^{1/3}}, \tag{1}$$

$$p_{\hat{k}}^{\text{head}} = K_{Ic}^{2/3}\Delta\gamma^{1/3}, \quad V_{\hat{k}}^{\text{head}} = Q_o t_{k\hat{k}} = \frac{K_{Ic}^{8/3}}{E'\Delta\gamma^{5/3}} = \ell_b^2 w_{\hat{k}}^{\text{head}}. \tag{2}$$

In the head, fluid flow is negligible such that according to Poiseuille's law,

$$\frac{\partial p}{\partial z} = \Delta\gamma$$

The head is divided into a rounded part where lateral expansion occurs and a bottom, laterally stationary part. Using a local coordinate system whose origin is centred at the boundary between the expanding and stationary part: $\tilde{z} = z - \ell_{\hat{k}}^{\text{head}}(\gamma^{\text{head}} - \lambda)$, in dimensionless form, the dimensionless pressure becomes

$$\Pi(\zeta, \xi) = \zeta - (\gamma^{\text{head}} - \lambda)$$

where γ^{head} the dimensionless head length scaled by ℓ_b and $\zeta = z/\ell_b$. The condition

$$K_I = K_{Ic}$$

is imposed for $\zeta \in [0, \lambda]$, while the breadth is constant for $\zeta < 0$ and given by $\beta\ell_b$, i.e.:

$$b(\zeta < 0)/\ell_b = \beta$$

where β is the unknown dimensionless breadth in the laterally stationary part and $\mathrm{d}b/\mathrm{d}\zeta = 0$ at $\zeta = 0$. Solving numerically the elasticity equation using a piece-wise constant displacement discontinuity method in combination with the previous constraints, Germanovich et al. [2014] arrives at the following solution for the total breadth of the fracture

$$b(\zeta > 0)/\ell_b = \beta\sqrt{1 - a(\zeta/\lambda)^2 - (1-a)(\zeta/\lambda)^4} \qquad a \approx 0.6967 \tag{3}$$

in the laterally spreading part, of the head with the following dimensionless extent of the laterally spreading region

$$\lambda \approx 1.3935 \times \left(0.249\sqrt{2/\pi}\right)^{2/3} \approx 0.4745$$

the dimensionless head size

$$\gamma^{\text{head}} \approx 5.19 \times \left(0.249\sqrt{2/\pi}\right)^{2/3} \approx 1.7671$$

and dimensionless breadth:

$$\beta \approx 2 \times (0.249\sqrt{2/\pi})^{2/3} \approx 0.6809 \approx \pi^{-1/3}.$$

We show that the evolution of the breadth in the head (over λ, equation (3)) matches our simulations in figures 2g - i by red dashed lines. In fine, the dimensional head breadth, length, net pressure and volume are respectively

$$\begin{aligned} b &\approx 0.6809\ell_b \approx \pi^{-1/3}\ell_b \\ \ell^{\text{head}} &\approx 1.7671\ell_b \\ p &\approx p_{\hat{k}}^{\text{head}} \times \left(z/\ell_b - (\gamma^{\text{head}} - \lambda)\right) \\ V^{\text{head}} &\approx 0.7008\ell_b^2 w_{\hat{k}}^{\text{head}} \end{aligned}$$

1.2 Viscous tail

The tail is modelled as a long finger-like hydraulic fracture for which the usual PKN hydraulic fracture model assumptions apply. Notably, the elastic relation can be written at the cross-section z

$$w(z, x) = 2\frac{bp(z)}{E'}\sqrt{1 - 4x^2/b^2} \qquad x \in [-b/2, b/2]$$

with p the net pressure. The average width of the cross section is related to the net pressure simplys as:

$$\bar{w}(z) = \pi\frac{bp(z)}{2E'}$$

The fluid flow in the tail is 1D,

$$\frac{\partial \bar{w}}{\partial t} + \frac{\partial q_z}{\partial z} = \delta(z) Q_o / b$$

and with a cross-sectional average of Poiseuille's law is:

$$q_z = -\frac{\bar{w}^3}{\pi^2 \mu} \left(\frac{\partial p}{\partial z} - \Delta\gamma \right)$$

In the viscous tail $\frac{\partial p}{\partial z} \ll \Delta\gamma$, such that

$$q_z \approx \frac{\bar{w}^3 \Delta\gamma}{\pi^2 \mu}.$$

and the global volume balance in the tail is

$$b \int_0^{\ell^{\text{tail}}} \bar{w} \mathrm{d}z = Q_o t - V^{\text{head}}$$

accounting for the constant volume of the head. Looking for a self-similar solution for which the average width $\bar{w}$ is uniform and constant in the tail and the velocity in the tail is constant such that

$$v_z = \frac{\mathrm{d}\ell^{\text{tail}}}{\mathrm{d}t} = q_z / \bar{w} = \frac{\bar{w}^2 \Delta\gamma}{\pi^2 \mu}.$$

The volume balance of the tail becomes

$$b \ell^{\text{tail}} \bar{w} = Q_o t - V_{head}$$

which provides the expression for the velocity in the tail:

$$\frac{\mathrm{d}\ell^{\text{tail}}}{\mathrm{d}t} = \frac{Q_o}{b\bar{w}} = \frac{\bar{w}^2 \Delta\gamma}{\pi^2 \mu}$$

such that we obtain

$$\bar{w} = \left(\pi^2 \frac{Q_o \mu}{b \Delta\gamma} \right)^{1/3} \qquad p = \frac{2E'}{\pi b} \left(\pi^2 \frac{Q_o \mu}{b \Delta\gamma} \right)^{1/3}$$

and

$$\ell^{\text{tail}} = \frac{Q_o t}{b\bar{w}} - \frac{V_{head}}{b\bar{w}}. \tag{4}$$

It is possible to rewrite equation (4) using the characteristic tail length $\ell_{\widehat{k}}$ as

$$\ell^{\text{tail}} = \frac{12^{1/3}}{\pi^{2/3} \beta^{2/3}} \ell_{\widehat{k}} - \frac{V_{head}}{b\bar{w}}$$

where we now replace V^{head} (with its numerical pre-factor) and $\overline{w}$ as defined previously and use by the scales in (1) using $\ell^{\text{tail}} = \gamma^{\text{tail}} \ell_b$ to obtain

$$\gamma^{\text{tail}} \approx \frac{12^{1/3}}{\pi^{2/3} \beta^{2/3}} \left(\frac{\Delta\gamma^{13/9} Q_o^{2/3} t}{K_{Ic}^{10/9} \mu'^{1/3}} - 0.7008 \frac{K_{Ic}^{14/9}}{\mu'^{1/3} Q_o^{1/3} \Delta\gamma^{2/9} E'} \right).$$

We now replace the time as $\tau = t / t_{k\widehat{k}}$ and note that

$$\mathcal{M}_{\widehat{k}}^{-1/3} = \frac{K_{Ic}^{14/9}}{\mu'^{1/3} Q_o^{1/3} \Delta\gamma^{2/9} E'}$$

such that we get

$$\gamma^{\text{tail}} \approx \frac{12^{1/3}}{\pi^{2/3} \beta^{2/3}} \mathcal{M}_{\widehat{k}}^{-1/3} \left(\tau - 0.7008 \right) \approx 1.3789 \mathcal{M}_{\widehat{k}}^{-1/3} \left(\tau - 0.7008 \right). \tag{5}$$

A comparison of our numerical simulations with this value is presented in table 1 of the main text.

We estimate from this equation the dimensionless time τ for which the dominant linear term will be valid within a given percentages. We pose the equation as

$$\varepsilon \frac{12^{1/3}}{\pi^{2/3}\beta^{2/3}} \mathcal{M}_{\widehat{k}}^{-1/3} \tau = \gamma^{\text{tail}} \rightarrow \tau_\varepsilon = \frac{0.7008}{1-\varepsilon}$$

where ε is the "error" between the linear term and the complete solution. We estimate the error to be within our maximum numerical error of 5% (e.g. $\varepsilon = 0.95$) such that we get a dimensionless time of

$$\tau_{0.95} = \left(t/t_{k\widehat{k}}\right)_{0.95} \approx 14.0$$

this limit for convergence is used within the main text section 4.2 to describe the transient .

It is now possible to derive the total fracture length by the addition of the head length to the tail length (5) as

$$\gamma^{\text{total}} = \gamma^{\text{tail}} + \gamma^{\text{head}} \approx 1.3789 \mathcal{M}_{\widehat{k}}^{-1/3} \left(\tau - 0.7008\right) + 1.7671$$

This expression for γ^{total} is plotted with green dashed lines in figure 2c of the main text. We additionally present the dominant term $1.3789 \mathcal{M}_{\widehat{k}}^{-1/3} \tau$ with green dashed-dotted lines.

We finally derive the scales of the opening and the pressure in the tail. According to Germanovich et al. [2014] they are given in their scaling as

$$p/p_* = \overline{w}/w_* = \left(\frac{Q_o/Q_*}{2\alpha}\right)^{1/3}$$

where $\overline{w}$ is the average opening in the tail. Transformed in our scaling these two quantities read

$$\frac{p}{1.3674 p_{\widehat{k}}^{\text{head}}} = 0.7281 \mathcal{M}_{\widehat{k}}^{1/3} \rightarrow p/p_{\widehat{k}}^{\text{head}} = 0.9956 \mathcal{M}_{\widehat{k}}^{1/3}$$

$$\frac{\overline{w}}{1.46264 w_{\widehat{k}}^{\text{head}}} = 0.7281 \mathcal{M}_{\widehat{k}}^{1/3} \rightarrow \overline{w}/w_{\widehat{k}}^{\text{head}} = 1.0650 \mathcal{M}_{\widehat{k}}^{1/3}.$$

From which we now can derive the maximum opening (at the centerline $x = 0$) as

$$w\left(0,z\right) = \frac{4}{\pi}\overline{w}\left(z\right) \rightarrow w\left(0,z\right)/w_{\widehat{k}}^{\text{head}} = 1.3559 \mathcal{M}_{\widehat{k}}^{1/3}.$$

1.3 Limit of applicability of their theory

Germanovich et al. [2014] argue that their solution is only valid as long as the breadth in the tail is stationary. To validate this condition, the pressure in the tail cannot exceed the value required for lateral fracturing (i.e. $p \leq K_{Ic}/\sqrt{\pi\beta\ell_b}$). This condition results in a dimensionless release rate in their contribution

$$Q/Q_* < 0.1761.$$

We can translate their dimensionless release rate into our scaling as

$$Q/Q_* = 0.1922 \mathcal{M}_{\widehat{k}}$$

such that the above inequality leads to the following limit

$$0.1922 \mathcal{M}_{\widehat{k}} < 0.1761 \rightarrow \mathcal{M}_{\widehat{k}} < 0.9159$$

which is reported as the limit of $\mathcal{M}_{\widehat{k}} \approx 0.92$ in section 6 of the main text.

2 Viscosity dominated solution in the source region

The scales presented by Lister [1990a] in equations 2.14 correspond qualitatively (upon numerical prefactors and by replacing t by solving $\ell(t) = z$ for t) to the scaling listed in equation 5.4 of the main text . We rederive their scaling using our parameters to plot the corresponding solutions in figures 5 and 6 of the main text. First, we can retrieve his scales using our characteristic fracture length

$$\ell_{\widehat{m}}(t) = z = \frac{\Delta\gamma^{1/2} Q_o^{1/2}}{E'^{1/6}\mu'^{1/3}} t^{5/6} \rightarrow t_z = \frac{E'^{1/5}\mu'^{2/5}}{\Delta\gamma^{3/5} Q_o^{3/5}} z^{6/5}$$

such that we obtain them as

$$b^{\text{Lister, 1990}}(z) = 0.6335 \times b_{\widehat{m}}(t = t_z) = 0.6335 \frac{Q_o^{1/10}\mu'^{1/10}E'^{3/10}}{\Delta\gamma^{4/10}} z^{3/10}$$

$$w^{\text{Lister, 1990}}(z) = 0.5086 \times w_{\widehat{m}}(t = t_z) = 0.5086 \frac{Q_o^{3/10}\mu'^{3/10}}{E'^{3/10}\Delta\gamma^{6/10}} z^{-1/10}$$

$$h^{\text{Lister, 1990}}(t) = 2.5698 \times \ell_{\widehat{m}}(t) = 2.5698 \times \frac{\Delta\gamma^{1/2} Q_o^{1/2}}{E'^{1/6}\mu'^{1/3}} t^{5/6}$$

It is now possible to get the breadth plotted in figure 5a of the main text by replacing $z = \zeta\ell_{\widehat{m}}(t)$, using the prefactors to his solution, and then dividing by our breadth scale

$$\frac{b^{\text{pseudo 3D}}(\zeta)}{b_{\widehat{m}}(t)} = 1.6629 \times \zeta^{3/10}$$

similarly, we can get the opening at the centerline, the opening profile (with $\xi = x/b_{\widehat{m}}$), and the cross-sectional volume as

$$\frac{w^{\text{pseudo 3D}}(\xi = 0, \zeta)}{w_{\widehat{m}}(t)} = 0.9197 \times \zeta^{-1/10}$$

$$\frac{w^{\text{pseudo 3D}}(\xi, \zeta)}{w_{\widehat{m}}(t)} = 0.9197 \times \left(1 - 0.3616 \frac{\xi^2}{\zeta^{3/5}}\right) \zeta^{-1/10}$$

$$\frac{\int_{-1}^{1} w^{\text{pseudo 3D}}(\xi, \zeta)\, \mathrm{d}\xi}{w_{\widehat{m}}(t)\, b_{\widehat{m}}(t)} = 1.8017 \zeta^{1/5}$$

The central opening and the 2D cross-sectional volume are respectively used in figures 5c and b of the main text. We give further their transition scale from viscosity- to toughness-dominated for buoyant fractures as

$$\ell_{mk}^{\text{Lister, 1990}} = 5.76 \times 10^{-4} \ell_{mk}.$$

The opening distribution used in figures 6c and d is scaled by the time-independent transition scales $\ell_{m\widehat{m}}$ and $w_{m\widehat{m}}$. The opening distribution in such scaling is interestingly exactly equivalent to the one presented previously.

3 Post-processing of the numerical results

3.1 Automatic evaluation of characteristic quantitites

All of the following is either performed by the PyFrac function *get_fracture_geometric_parameters()* or *get_fracture_head_volume()*.

Global quantitites The numerical data of PyFrac [Zia and Lecampion, 2020] includes the intersections of the fracture front $\mathcal{C}(t)$ with the cell edges (c.f. figure (1)).We extract from these points the fracture breadth vector at the locations z_i as $\mathbf{b}(\mathbf{z}, t)$ from the subtraction between the intersections on the positive (i.e. where $x_i > 0$) and the negative side (i.e. where $x_i < 0$). In the vector notation, we have $\mathbf{z}$ as the vector of all the intersections of the front with a discrete cell edge on the z-axis. There is no ambiguity in this evaluation as

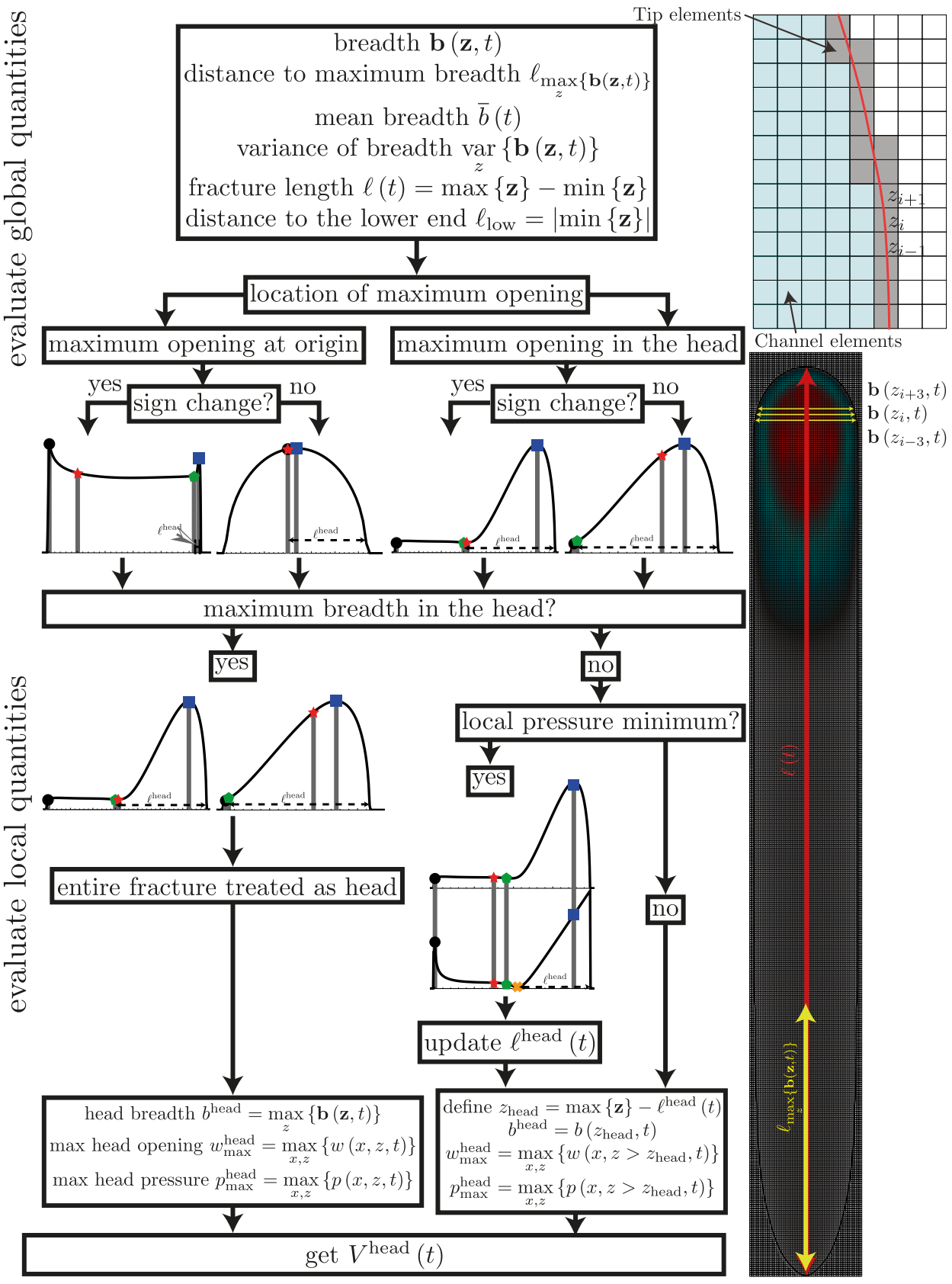

Figure 1: Flow chart of numerical evaluation. Black circles mark the origin, blue squares are max head opening, red stars distance to the maximum breadth, green polygons location of the head evaluated by the "opening method", and yellow cross the update with the pressure check.

the release point is chosen as $(x, z) = (0, 0)$ and needs to be at a cell centre, and the $z-$axis is an axis of symmetry of the problem.

From the breadth we obtain the maximum breadth by simply taking the maximum of $\mathbf{b}(\mathbf{z}, t)$. Note that as between two edge intersections the connection is a straight line. We ensure that the maximum breadth evaluated as such is actually the maximum breadth in the simulation. We then also estimate the distance to the maximum breadth as

$$\ell_{\max_z\{\mathbf{b}(\mathbf{z},t)\}} = \min\left\{z_i \in \mathbf{b}(\mathbf{z}, t) \geq 0.975 \cdot \max_z\{\mathbf{b}(\mathbf{z}, t)\}\right\}.$$

We acknowledge a variation of 2.5% along the breadth as numerical noise. To stabilize the scheme, notably for toughness-dominated cases, we thus decide to take the distance to the maximum breadth as the smallest value of an intersection z_i where the breadth exceeds 97.5% of its maximum observed. This further allows us to get an average breadth $\bar{b}(t)$ and a variance of the breadth $\operatorname{var}_z\{\mathbf{b}(\mathbf{z}, t)\}$.

The fracture height is evaluated as the distance between the maximum vertical extent and the minimum vertical extent,

$$\ell(t) = \max\{\mathbf{z}\} - \min\{\mathbf{z}\}.$$

The last quantity we measure is the distance to the lower end of the fracture from the release point (i.e. the downward growth of the fracture) as $\ell_{\text{low}} = |\min\{\mathbf{z}\}|$.

Some of the quantities are displayed in figure 1. See also the sketch of figure 1 of the main text.

Local quantities We are mainly interested in the quantities within the head of the fracture. To achieve those we need first to decide if a head exists and what its extent is. To do so we get the pressure and opening profiles along the centerline of the fracture (e.g. $w(x = 0, z, t)$) evaluated at the cell center. We then search for the release point (i.e. $z = 0$) and get the location of the overall maximum opening $\max_z\{w(x = 0, z, t)\}$. We check if the maximum opening is at the origin (with a security margin of 4 cells around the origin) or elsewhere.

1. **Maximum opening at the origin:** If the maximum opening is at the origin, we check for a sign change in the derivative of the opening between the origin and the top of the fracture. If we do not have such a case the opening monotonically decreases from the injection point to the fracture tip and we do not have a head as such. In this case, we evaluate the head length $\ell^{\text{head}}(t)$ as

   $$\ell^{\text{head}}(t) = \max\{\mathbf{z}\} \quad \text{if no head exists.}$$

   If the decrease between the release point and the fracture tip exists, we check for the location where the opening starts to increase again towards the fracture tip. This allows us to define the location of the maximum opening in the head, which is further away than the previously mentioned change of slope but still inside the fracture. In between this maximum opening and the location where fracture breadth starts to increase again must necessarily be at least two inflexion points. We take the first inflexion point from the sign change in the opening as the location of the head length (the second is where the opening slope starts to decrease towards the head).

2. **Maximum opening in the head:** If the maximum opening is not at the origin, it must be in the head. If such is the case, we search for a sign change between the origin and the maximum opening and proceed as previously described. There might not be any sign change (flat tail above the release point). In the configuration without sign change, we directly search for all inflexion points and take the one second closest to the maximum opening in the head (the closest one would be where the slope of the opening starts to decrease towards the head).

The just described evaluation method is called the "opening method" from here on.

We perform a "check" using the pressure distribution on all opening method evaluations. The primordial usage of the opening is favoured because our scheme provides a better estimate of opening than pressure. For the pressure "check", we first evaluate if the maximum breadth occurs in the head using the head length defined via the "opening method". If such is the case, we chose the head breadth $b^{\text{head}}(t) = b\left(z_{tip}(t) - \ell^{\text{head}}(t), t\right)$ as the maximum breadth to reduce numerical noise in our results. If a head exists, we check if a local pressure minimum exists inside the previously evaluated head. If so, we redefine the beginning of the head from this local minimum to the tip. Otherwise we leave the evaluation unchanged.

The maximum head opening and pressure are then defined according to our evaluation of the head dimensions, and the breadth is calculated as

$$b^{\text{head}}(t) = b\left(z_{tip}(t) - \ell^{\text{head}}(t), t\right).$$

It remains for us to obtain the volume of the head. We obtain this by a simple summation over the elements contained in the head. We define the channel e_{ci}^{head} channel means fully inside the fracture, c.f. figure 1) and the tip e_{ti}^{head} (elements where the front passes, c.f. figure 1) elements in the head using the previously obtained dimensions of the head. The volume in the head is then simply given by

$$V^{\text{head}}(t) = A_e \left\{ \sum_{i=1}^{n_c} w\left(x\left(e_{ci}\right), z\left(e_{ci}\right), t\right) + \sum_{j=1}^{n_t} f\left(e_{tj}\right) w\left(x\left(e_{tj}\right), z\left(e_{tj}\right), t\right) \right\}$$

where A_e is the (uniform) element area, and f the filling fraction of the tip element. The filling fraction is the percentage of the area which is occupied by the fracture.

3.2 Definition of uniform breadth

The distinction between uniform and non-uniform breadth is based on a post-processing evaluation within Mathematica. The evaluation is performed on the last time-step of the simulation. From the post-processing within PyFrac [Zia and Lecampion, 2020], we know where the head starts and where the maximum breadth is located. On the footprint, we thus extract the breadth in between as the breadth of the tail

$$b^{\text{tail}}\left(z^{\text{tail}}, t\right) \quad \text{for } \ell_{\max_z\{\mathbf{b}(\mathbf{z},t)\}} \leq z^{\text{tail}} \leq z_{tip} - \ell^{\text{head}}(t).$$

This is the domain for which the breadth would need to be uniform for the fracture to be classified as finger-like. We recall that we defined the distance to the maximum breadth with a 2.5% margin. In our decision regarding a uniform breadth, we need to account for this uncertainty. We define our decision upon the breadth being uniform using the maximum difference in breadth in the tail

$$\frac{\max_z \left\{b^{\text{tail}}\left(z^{\text{tail}}, t\right)\right\} - \min_z \left\{b^{\text{tail}}\left(z^{\text{tail}}, t\right)\right\}}{\max_z \left\{b^{\text{tail}}\left(z^{\text{tail}}, t\right)\right\}} \leq 0.04$$

which corresponds to a 4% relative difference. If we subtract the 2.5% error already included due to the evaluation of the distance. This leaves us with a maximum variation of 1.5% that we accept. This evaluation is used to obtain figure 8 of the main text and defines the discussion of uniform (finger-like) vs non-uniform (inverted cudgel) breadth.

4 2D steadily moving semi-infinite buoyant hydraulic fracture solver

We derive from the two-dimensional formulation the following scales

$$\ell_b^{\text{2D}} = \frac{E'^{1/2} Q_{2D}^{1/6} \mu'^{1/6}}{(\Delta\rho g)^{2/3}}, \quad w_b^{\text{2D}} = \frac{Q_{2D}^{1/3} \mu'^{1/3}}{(\Delta\rho g)^{1/3}}, \quad p_b^{\text{2D}} = E'^{1/2} Q_{2D}^{1/6} \mu'^{1/6} (\Delta\rho g)^{1/3} \tag{6}$$

and a dimensionless toughness

$$\kappa = \frac{K_{Ic}}{E'^{3/4} \mu'^{1/4} Q_o^{1/4}}$$

where the 2D release rate is obtained using $Q_{2D} = v_{z*} w_*$. This leads us to the following set of scaled equations for the 2D semi-infinite fracture

$$\Pi^{\text{2D}}\left(\widehat{\xi}^{\text{2D}}\right) = \frac{1}{4\pi} \int_0^\infty \frac{\partial \Omega}{\partial \hat{\eta}^{\text{2D}}} \frac{\mathrm{d}\hat{\eta}^{\text{2D}}}{\hat{\xi}^{\text{2D}} - \hat{\eta}^{\text{2D}}} \quad \text{elasticity}$$

$$1 = \Omega^2 \left(\frac{\partial \Pi}{\partial \hat{\xi}^{\text{2D}}} + 1\right) \quad \text{lubrication}$$

$$\Omega = \sqrt{\frac{32}{\pi}} \kappa \left(\hat{\xi}^{\text{2D}}\right)^{1/2} \qquad \hat{\xi}^{\text{2D}} \ll 1 \quad \text{LEFM}$$

where $\widehat{\xi}^{2D} = \widehat{x}/\ell_b^{2D}$ is the scaled distance to the tip with $\widehat{x} = v_{z*}t - z$ the tip based coordinate.

The two-dimensional semi-infinite buoyant hydraulic fracture is now solved via a numerical scheme based on a Gauss-Chebyshev quadrature. Using this approach for elastic boundary integral equations is well established [Erdogan et al., 1973] and has been used for similar problems before [Viesca and Garagash, 2018, Moukhtari and Lecampion, 2018]. We follow mainly the developments presented in Moukhtari and Lecampion [2018], albeit including the buoyant stress gradient. The same discretization method is chosen such that one has

$$\frac{\partial \Omega}{\partial \hat{\xi}^{2D}} = \sqrt{\frac{32}{\pi}} \frac{\kappa}{\hat{\xi}^{2D}} + \sqrt{\hat{\xi}^{2D}} \phi\left(\hat{\xi}^{2D}\right) \tag{7}$$

with $\phi\left(\hat{\xi}^{2D}\right)$ the unknown, non-singular dislocation density represented as a Chebyshev polynomial. This approach allows us to naturally embed the LEFM condition in the discretization, which will thus automatically be verified. We solve for the values of the Chebyshev polynomal using third kind Gauss-Chebyshev polynomial which use two sets of nodes $\mathbf{v} = \{v_j\}$ with $j = 1, ..., n$ and $\mathbf{u} = \{u_i\}$ with $i = 1, ..., n$. The use of third kind polynomials directly declines from equation (7), as naturally the corresponding weight function $\omega(s)$ appears after the following variable transformation [Ioakimidis and Theocaris, 1980, Viesca and Garagash, 2018]

$$\hat{\xi}^{2D} = \frac{1+v}{1-v}, \quad \omega(s) = \sqrt{\frac{1+v}{1-v}}.$$

The related set of points, corresponding to the roots of the third and fourth Chebyshev polynomials respectively, are given as

$$v_j = \cos\left(\frac{\pi j}{n+1/2}\right), j = 1, .., n; \qquad u_i = \cos\left(\frac{\pi i}{n+1/2}\right), i = 1, ..., n.$$

This allows us to discretize the elasticity equation as

$$\frac{\Pi^{2D}\left(\widehat{\xi}_j^{2D}\right)}{1-v_j} = \frac{1}{4\pi} \sum_i^n \frac{A_i}{1-u_i} \frac{\phi\left(\hat{\xi}_j^{2D}\right)}{v_j - u_j}$$

where $\widehat{\xi}_j^{2D} = \widehat{\xi}^{2D}(v_j)$ and $A_i = \pi(1+u_i)/(n+1/2)$ is the quadrature weight. From this equation, we create the following elasticity matrix

$$\mathbb{K}_{ij} = \frac{1}{4\pi} \sum_i^n \frac{A_i}{1-u_i} \frac{1-v_j}{v_j - u_j}.$$

The lubrication equation is discretized via a finite difference scheme at the mid-points $\widehat{\xi}_{j+1/2}^{2D}$

$$\Omega\left(\widehat{\xi}_{j+1/2}^{2D}\right)^2 \left\{ \frac{\Pi^{2D}\left(\widehat{\xi}_{j+1}^{2D}\right) - \Pi^{2D}\left(\widehat{\xi}_j^{2D}\right)}{\widehat{\xi}_{j+1}^{2D} - \widehat{\xi}_j^{2D}} + 1 \right\} = 1 \tag{8}$$

where we recall that due to equation (7), the opening is given by

$$\Omega\left(\widehat{\xi}_{j+1/2}^{2D}\right) = \sqrt{\frac{32}{\pi}} \kappa \widehat{\xi}_{j+1/2}^{2D} + \phi\left(\hat{\xi}_{j+1/2}^{2D}\right). \tag{9}$$

Note that we obtain $\phi\left(\hat{\xi}_{j+1/2}^{2D}\right)$ by linear interpolation of $\phi\left(\hat{\xi}^{2D}\right)$. We need now to set a single last condition to close the system, which we choose as a zero pressure condition at infinity $\Pi^{2D}\left(\widehat{\xi}_n^{2D}\right) = 0$. The problem is then solved via the built-in Mathematica find root function using a quasi-Newton method with a finite difference approximation of the jacobian. The sequence to solve the problem is then as follows:

1. Create the discretization with the elasticity matrix $\mathbb{K}$ and the interpolation function of $\phi\left(\hat{\xi}_{j+1/2}^{2D}\right)$
2. Give an initial estimate of the pressure. The estimate of the initial pressure is performed step-wise:

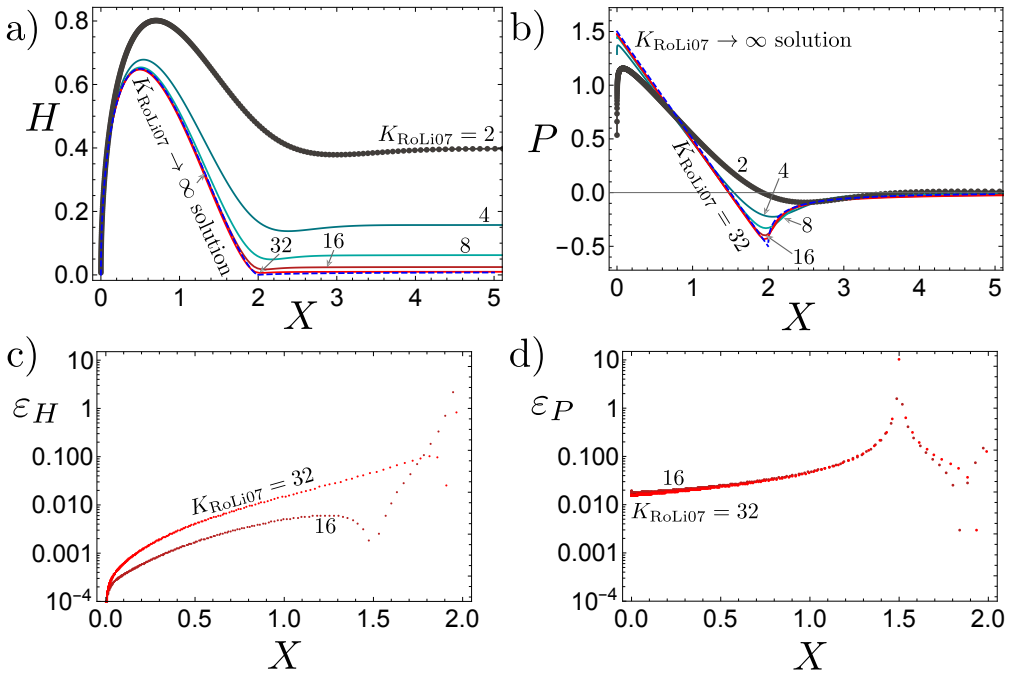

Figure 2: 2D semi-infinite opening (a) and pressure (b) in the scaling of equation (11). Blue-dashed lines correspond to the solution of Roper and Lister [2007] for $K_{\mathrm{RoLi07}} = 32$ (equations (12)). Simulation with $K_{\mathrm{RoLi07}} = 2$ shows the evaluation points as markers. Relative error ((c) opening and (d) pressure) of our numerical evaluation with the solutions (12).

(a) We use the so-called viscosity asymptote (Desroches et al. [1994]) as an initial guess for a value of $\kappa \approx 0.16$, which we know to have a good convergence. We then stepwise reduce its value to $\kappa \approx 0.02$, using the previously obtained pressure distribution as an initial guess.

(b) Depending on the value of κ in our problem, we choose the closest corresponding pressure distribution. The value of $\kappa \approx 0.02$ is sufficient to get a good convergence for the solver even when $\kappa = 0$ in the zero toughness case.

3. Solve iteratively until the residual convergence (Accuracy Goal of Mathematica set to 8):

(a) We use the built-in linear solve function of Mathematica to solve the equation

$$\Pi^{\mathrm{2D}} = \mathbb{K} \cdot \phi$$

at the discrete points for $\phi\left(\hat{\xi}_j^{\mathrm{2D}}\right)$.

(b) Evaluate the opening at the mid-points by equation (9).

(c) Use equation (8) to build a residual.

(d) Estimate the new pressure distribution from the residual and restart at (a)

Note: The K_* used in the code is directly equal to

$$K_* = \sqrt{\frac{32}{\pi}}\kappa.$$

4.1 Validation with limiting solutions

Large-toughness limit The large toughness limit has been solved in the article Roper and Lister [2007]. However, to compare, we need to make our scales equivalent, which requires some additional steps. We have the following equivalencies between their and our scales

$$\widehat{x} = \frac{1}{2}\ell_b^{\mathrm{2D}}, \quad \widehat{h} = \frac{1}{2}w_b^{\mathrm{2D}}, \quad \widehat{p} = \frac{1}{2}, \quad K_{\mathrm{RoLi07}} = \frac{1}{2}\sqrt{\frac{32}{\pi}}\kappa = \frac{1}{2}K_* \tag{10}$$

where K_{RoLi07} is their dimensionless toughness as in equation 2.10. We further need to pay attention that their opening h equals to our $w/2$. Roper and Lister [2007] then rescale those parameters again to obtain

$$X = \frac{x/\widehat{x}}{K_{\text{RoLi07}}^{2/3}} = \frac{2 \cdot 2^{2/3}\, x/\ell_b^{2\text{D}}}{K_*^{2/3}}, \quad H = \frac{h/\widehat{h}}{K_{\text{RoLi07}}^{4/3}} = \frac{2^{4/3}\, w/w_b^{2\text{D}}}{K_*^{4/3}}, \quad P = \frac{p/\widehat{p}}{K_{\text{RoLi07}}^{2/3}} = \frac{2 \cdot 2^{2/3}\, p/p_b^{2\text{D}}}{K_*^{2/3}} \tag{11}$$

They now derive an approximated solution for the opening and pressure in this scaling. The output of our numerical solver is the scaled coordinates $x/\ell_b^{2\text{D}}$, opening $w/w_b^{2\text{D}}$, and pressure $p/p_b^{2\text{D}}$.

We use as a comparison and validation of our code the opening with the first order tail correction and the zero-order pressure

$$\begin{aligned} H &= \frac{1}{2} X^{1/2} (2 - X)^{3/2} + \mathcal{H}(x-2)\, K_{\text{RoLi07}}^{-4/3} \sqrt{2} \frac{X^{1/4} (x-2)^{3/4}}{(2x^2 - 2x - 1)^{1/2}} \\ P &= \frac{3}{2} - X + \mathcal{H}(x-2)\, \frac{(2X-1)(X-2)^{1/2}}{2X^{1/2}} \end{aligned} \tag{12}$$

where $\mathcal{H}$ is the Heaviside theta function. We compare the solutions graphically in figures 2a and b and present the errors in the head obtained for an evaluation with $n = 400$ and $\kappa \approx 10, 20$ ($K_{\text{RoLi07}} = 16, 32$) in figures 2c and d. Note that we present the relative error which explains the increase when approaching the zero in pressure at $X \approx 1.5$. The absolute error in this range is small if we compare it using figure 2b Generally, the relative error remains within a few per cent except towards the end of the head. This can be explained by the enforced continuity of our model as opposed to the Heaviside functions present in the analytical solutions (12). Additionally, one observes that the error on the opening increases towards the transition from the head to the tail. The reason is that the corrected head solution tends to 0 at $X = 2$ whereas our solution is continuous. The match between the solutions in the tail is then again well visible when comparing the opening at values of $X \gg 2$.

Zero-toughness limit TTo ensure that the code also works in the other limit of zero-toughness we compare the results to the numerical results with $K_* = 0$ presented in figure 3 of Lister [1990b]. This data is picked numerically and then rescaled from the scales provided in the figure. Figure 2 is comparing graphically our opening profile for a simulation with $K_* = K_{\text{RoLi07}} = \kappa = 0$ in "our" scales (6). Generally, the match is nearly perfect except around the maximum opening. Around maximum opening the picking of the data from the figure was very difficult as the resolution there made it very hard to determine the exact location of the graph. Nonetheless, the very good match elsewhere as well as the correspondence for the toughness-dominated case, allow us to conclusively state that our numerical 2D Gauss-Chebyshev solver of the semi-infinite fracture is valid for the entire range of κ possible.

5 Comparison with experiments

5.1 Heimpel and Olson (1994)

We try to compare the experimental investigations performed by Heimpel and Olson [1994] with our numerical results. The equivalent solid and fluid properties of their experiments are reported in table 1. The plain strain modulus E' is derived from their shear modulus G with the assumption of a Poisson's coefficient of $\nu \approx 0.5$ (also estimated by them) as

$$E' = \frac{2G(1+\nu)}{1-\nu^2}.$$

The toughnesses reported are the ones they obtain using a critical volume. It is interesting to note that this critical volume corresponds to our toughness-dominated head volume $V_{\widehat{k}}^{\text{head}}$ (see equation 4.1 of the main text). We infer this correspondence because our simulations present a similar kink in the velocity (see figure 10a of the main text) as observed in their experiments. Using this resemblance, we can estimate the fracturing toughness from the critical volume as

$$V^{\text{c}} = \frac{K_{Ic}^{8/3}}{E' \Delta\gamma^{5/3}} \rightarrow K_{Ic}^{\text{c}} = (V^{\text{c}})^{3/8}\, E'^{3/8} \Delta\gamma^{5/8}$$

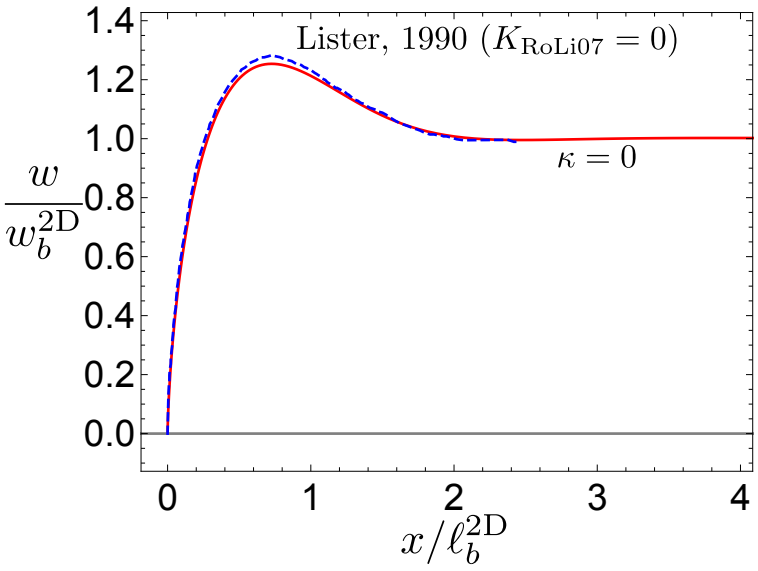

Figure 3: Comparison between the zero-toughness solution extracted from Lister [1990a] figure 2 (blue-dashed line) with our zero-toughness Gauss-Chebyshev evaluation (red line).

Gelatines					
Concentration	G [Pa]	K_{Ic} $[\mathrm{Pa}\cdot\sqrt{\mathrm{m}}]$	ν [-]	ρ_s $[\mathrm{kg}\cdot\mathrm{m}^{-3}]$	E' [Pa]
1.4%	190	15	0.5	1000	760
1.6%	276	19			1104
1.8%	355	23			1420
4.0%	2150	114			8600
Fluids					
Fluid type	μ [Pa · s]	g' $[\mathrm{m}\cdot\mathrm{s}^{-2}]$	μ' [Pa · s]	$\Delta\gamma$ $[\mathrm{Pa}\cdot\mathrm{m}^{-1}]$	
Air	10^{-5}	9.8	1.2×10^{-4}	9.8×10^{3}	
Hexane	10^{-4}	3.4	1.2×10^{-3}	3.4×10^{3}	
1 Cst silicon Oil	10^{-3}	1.8	1.2×10^{-2}	1.8×10^{3}	
Mineral Oil	10^{-1}	1.5	1.2	1.5×10^{3}	
Corn syrup solution	5×10^{0}	−4.1	6×10^{1}	-4.1×10^{3}	
Corn syrup/cadmium	5×10^{0}	1.41	6×10^{1}	-1.41×10^{3}	
Mercury	10^{-3}	−126	1.2×10^{-2}	-1.26×10^{5}	

Table 1: Properties of the solids and the fluids used in the experiments of Heimpel and Olson [1994]. The parameters after the double boundary are estimated or derived and not explicitly reported in Heimpel and Olson [1994].

where we use the superscript $\cdot^{\mathrm{c}}$to indicate the critical volume. We report the result in table 2 and observe an acceptable match between the two approaches.

For the fluids, a buoyancy g' is reported. From their reported values we obtain our $\Delta\gamma$ with the assumption of a gelatine density akin to the density of water $\rho_s \approx 1000 \left[\mathrm{kg} \cdot \mathrm{m}^{-3}\right]$

$$g' = \frac{\Delta\gamma}{\rho_s} \rightarrow \Delta\gamma = \rho_s g'.$$

Velocity comparison

For a series of experiments, Heimpel and Olson [1994] report the injected volume and fracture velocity (their figure 2). We extract the values of this visualization and scale the results with our $\widehat{\mathrm{K}}$ head scales (see equation 4.1 of the main text) as follows

$$\frac{V}{V_{\widehat{k}}^{\mathrm{head}}} = \frac{Q_o E' \Delta\gamma^{5/3} t}{K_{Ic}^{8/3}} = \frac{t}{t_{k\widehat{k}}}$$
$$\frac{U}{\partial \ell_{\widehat{k}}(t)/\partial t} = \frac{\dot{\ell}(t)}{\dot{\ell}_{\widehat{k}}} = \dot{\ell}(t) \frac{Q_o^{2/3} \Delta\gamma^{7/9}}{K_{Ic}^{4/9} \mu'^{1/3}}$$

where we estimate the unknown Q_o for laboratory experiments as $Q_o = 1. \times 10^{-8} \left[\mathrm{m}^3 \cdot \mathrm{s}^{-1}\right]$. We can thus obtain our numerical velocity using the time steps and increments of height (i.e. $\dot{\ell}(t_i) \approx (\ell_i - \ell_{i-a}) / (t_i - t_{i-1})$) and compare it to their values of U reported in figure two. Similarly, the volume of the abscissa of their figure 2 can be transformed into a dimensionless time using their parameters for the experiments. The so obtained figure is shown in the main text as figure 10a overlayed with three numerical simulations.

We report for the experiments the obtained value of the dimensionless viscosity $\mathcal{M}_{\widehat{k}}$ (equation 3.8 of the main text) to derive the length necessary to overcome the transient phase

$$\ell_{\mathrm{t}} \approx 19 \mathcal{M}_{\widehat{k}}^{-1/3} \ell_b.$$

In table 2, this value is compared with the sample height H_s. We observe that generally, the distance to overcome the transient is much larger than the sample size. This indicates that boundary effects due to the finiteness of the sample, as well as the initiation condition (which is poorly known) significally influence the results.

5.1.1 Breadth comparison

In figure 10b of the main text, we compare three values of fracture breadth from this contribution to the limiting breadth of the $\widehat{\mathrm{K}}$-solution of Germanovich et al. [2014]. The breadth values used are extracted from figures 8 and 9 of Heimpel and Olson [1994]. We list the values in table 3 along with their relative error.

5.2 Taisne and Tait (2009)

We use the table of breadths reported in Taisne and Tait [2009] to compare their breadth to the predicted breadth from the $\widehat{\mathrm{K}}$-solution of Germanovich et al. [2014]. We use their values of the Young's modulus reported in table 1 and again estimate the Poisson's coefficient of the gelatine as $\nu \approx 0.5$. As they directly report $\Delta\rho$, we obtain the buoyancy $\Delta\gamma$ by simple multiplication with the earth acceleration $g = 9.81 \left[\mathrm{m} \cdot \mathrm{s}^{-2}\right]$. We document our values in table 4, where the experiment N° corresponds to the value reported in table 1 of Taisne and Tait [2009]. The definitions of b^{obs} and b^{pred} are as in table 3.

Experiments of Heimpel and Olson [1994]								
Solid	Fluid	$V^{\mathrm{c}}\ [\mathrm{m}^3]$	$K_{Ic}^{\mathrm{c}}\ [\mathrm{Pa}\cdot\sqrt{\mathrm{m}}]$	$\overline{K_{Ic}^{\mathrm{c}}}\ [\mathrm{Pa}\cdot\sqrt{\mathrm{m}}]$	$1-K_{Ic}/\overline{K_{Ic}^{\mathrm{c}}}\ [\%]$	ℓ_{t}/H_s [-]	$Q_o\ [\mathrm{m}^3]$	$\mathcal{M}_{\widehat{k}}$ [-]
1.4%	Air	$4.\times10^{-7}$	15	15	0.11	55.6	10^{-8}	7.8×10^{-7}
1.6%	Air	$6.\times10^{-7}$	20	24.4	22.1	64.8		$8.\times10^{-7}$
1.6%	Hexane	$6.\times10^{-6}$	25			77.0		3.9×10^{-6}
1.6%	Mineral Oil	1.5×10^{-5}	21			15.9		2.3×10^{-3}
1.6%	Mercury	$3.\times10^{-8}$	32			1.44		4.4×10^{-4}
1.8%	Air	$1.\times10^{-6}$	27	27	13.9	77.0		$7.\times10^{-7}$
1.8%	Corn syrup/cadmium	continuous release				5.43		9.5×10^{-2}
4.0%	Air	$1.\times10^{-5}$	124	124	8.39	446		$8.8.\times10^{-8}$

Table 2: Combinations used for the experiments reported in Heimpel and Olson [1994] and characteristic values derived.

Breadth evaluation				
Solid	Fluid	Measured breadth b^{obs} [cm]	Predicted breadth $b^{\text{pred}} \approx \pi^{-1/3}\ell_b$ [cm]	$\left\lvert 1 - b^{\text{obs}}/b^{\text{pred}} \right\rvert$ [%]
1.4%	Air	1.5	0.9	65.4
1.8%	Corn syrup/cadmium	5.6	4.4	27.5
4.0%	Air	5.2	3.5	48.3

Table 3: Comparison of finger-like toughness-dominated fracture breadth with the experiments of Heimpel and Olson [1994] shown in their figures 8 and 9.

Experiments of Taisne and Tait [2009]									
experiment N°	E [Pa]	$\Delta\rho$ $[\mathrm{kg \cdot m^{-3}}]$	b^{obs} [cm]	ν [-]	E' [Pa]	K_{Ic} $[\mathrm{Pa \cdot \sqrt{m}}]$	$\Delta\gamma$ $[\mathrm{Pa \cdot m^{-1}}]$	b^{pred} [cm]	$\lvert 1 - b^{\mathrm{obs}}/b^{\mathrm{pred}} \rvert$ [%]
7	5352	240	11.6		7136.00	69.50	2354.4	6.52	77.87
8	5352	240	8.2		7136.00	69.50	2354.4	6.52	25.7
9	1544	103	7.4		2058.67	37.32	1010.4	7.57	2.29
10	1544	240	9.6		2058.67	37.32	2354.4	4.31	122
11	6950	240	6.7		9266.67	79.20	2354.4	7.11	5.83
12	2338	102	1.14		3117.33	45.94	1000.6	8.75	30.2
14	1787	102	8.1		2382.67	40.16	1000.6	8.00	1.20
15	2129	102	8.0		2838.67	43.83	1000.6	8.48	5.71
16	1903	373	6.2	0.5	2537.33	41.44	3659.1	3.44	80.1
17	1903	373	4.8		2537.33	41.44	3659.1	3.44	39.4
20	1843	255	5.8		2457.33	40.78	2501.6	4.39	32.1
22	2770	373	7.01		3693.33	50.00	3659.1	3.90	79.6
23	2770	373	7.25		3693.33	50.00	3659.1	3.90	85.8
24	2770	373	3.3		3693.33	50.00	3659.1	3.90	15.4
25	1102	373	6.0		1469.33	31.54	3659.1	2.87	109
26	3402	373	8.5		4536.00	55.41	3659.1	4.18	103
28	3402	186	7.6		4536.00	55.41	1824.7	6.65	14

Table 4: Breadth comparison for the finite volume release experiments of Taisne and Tait [2009].

References

J. Desroches, E. Detournay, B. Lenoach, P. Papanastasiou, J. R. A. Pearson, M. Thiercelin, and A. Cheng. The crack tip region in hydraulic fracturing. *Proceedings of the Royal Society of London. Series A: Mathematical and Physical Sciences*, 447(1929):39, 1994. ISSN 1364-5021. URL `http://rspa.royalsocietypublishing.org/content/447/1929/39.short`.

F Erdogan, G D&amp Gupta, and TS Cook. Numerical solution of singular integral equations. In *Methods of analysis and solutions of crack problems*, pages 368–425. Springer, 1973.

L. N. Germanovich, D. I. Garagash, L. Murdoch, and Robinowitz M. Gravity-driven hydraulic fractures. In *AGU Fall Meeting Abstracts*, volume 2014, pages H53C–0874, 2014.

M. Heimpel and P. Olson. Chapter 10 Buoyancy-Driven Fracture and Magma Transport through the Lithosphere: Models and Experiments. In Michael P. Ryan, editor, *Magmatic Systems*, volume 57 of *International Geophysics*, pages 223–240. Academic Press, 1994. doi: https://doi.org/10.1016/S0074-6142(09)60098-X.

N.I. Ioakimidis and P.S. Theocaris. The practical evaluation of stress intensity factors at semi-infinite crack tips. *Engineering Fracture Mechanics*, 13(1):31 – 42, 1980. ISSN 0013-7944. doi: https://doi.org/10.1016/0013-7944(80)90038-7. URL `http://www.sciencedirect.com/science/article/pii/0013794480900387`.

J. R. Lister. Buoyancy-driven fluid fracture: similarity solutions for the horizontal and vertical propagation of fluid-filled cracks. *J. Fluid Mech.*, 217:213–239, 1990a. doi: 10.1017/S0022112090000696.

J.R. Lister. Buoyancy-driven fluid fracture: the effects of material toughness and of low-viscosity precursors. *J. Fluid Mech.*, 210:263–280, 1990b.

F. E. Moukhtari and B. Lecampion. A semi-infinite hydraulic fracture driven by a shear thinning fluid. *J. Fluid Mech.*, 838:573–605, 2018. doi: 10.1017/jfm.2017.900.

S. M. Roper and J. R. Lister. Buoyancy-driven crack propagation: the limit of large fracture toughness. *J. Fluid Mech.*, 580:359–380, 2007.

B. Taisne and S. Tait. Eruption versus intrusion? Arrest of propagation of constant volume, buoyant, liquid-filled cracks in an elastic, brittle host. *J. Geophys. Res. Solid Earth*, 114(B6), 2009.

R. C. Viesca and D. I. Garagash. Numerical methods for coupled fracture problems. *Journal of the Mechanics and Physics of Solids*, 113:13–34, 2018.

H. Zia and B. Lecampion. PyFrac: A planar 3D hydraulic fracture simulator. *Comput. Phys. Commun.*, page 107368, 2020. ISSN 0010-4655. doi: https://doi.org/10.1016/j.cpc.2020.107368.